Ultrananocrystalline Diamond Membranes for Detection of High-Mass Proteins

H. Kim, J. Park, Z. Aksamija, M. Arbulu, and R. H. Blick

Phys. Rev. Applied **6**, 064031 — Published 30 December 2016

DOI: 10.1103/PhysRevApplied.6.064031

Ultra-Nano-Crystalline Diamond Nanomembranes

for High-Mass Protein Detection

H. Kim[1], J. Park[2], Z. Aksamija[3], M. Arbulu[4*] and R.H. Blick[1,5]

[1]*Department of Electrical and Computer Engineering, University of Wisconsin-Madison, 1415 Engineering Drive, Madison, WI 53706, USA*

[2]*Department of Electrical Engineering, Kyungpook National University, Daegu, Korea*

[3]*Department of Electrical and Computer Engineering, University of Massachusetts-Amherst, 100 Natural Resources Drive, Amherst, MA 01003, USA*

[4]*CIC-nanoGUNE, Tolosa Hiribidea 76, Donostia – San Sebastian, Spain*

[5]*Center for Hybrid Nanostructures (CHyN) & Institute of Applied Physics, University of Hamburg, Jungiusstrasse 11c, 20355, Hamburg, Germany*

[*] Corresponding author: maria@prospero-biosciences.com

ABSTRACT

Mechanical resonators realized on the nanoscale by now offer applications in mass sensing of bio-molecules with extraordinary sensitivity. The general idea is that perfect mechanical mass sensors should be of extremely small size to achieve zepto- or yocto-gram sensitivity in weighing single molecules similar to a classical scale. However, the small effective size and long response time for weighing biomolecules with a cantilever restricts their usefulness as a high-throughput method. Commercial mass spectrometry (MS) on the other hand, such as electro-spray ionization (ESI)-MS and matrix-assisted laser desorption/ionization (MALDI)-time of flight (TOF)-MS and their charge amplifying detectors are the gold standards to which nanomechanical resonators have to live up to. These two methods rely on the ionization and acceleration of biomolecules and the following ion detection after a mass selection step, such as time-of-flight (TOF). The principle we are describing here for ion detection is based on conversion of kinetic energy of the biomolecules into thermal excitation of CVD diamond nanomembranes via phonons, followed by phonon-mediated detection via field emission of thermally emitted electrons. We fabricated ultrathin diamond membranes with large lateral dimensions for MALDI-TOF MS of high mass proteins. These diamond membranes are realized by straightforward

etching methods based on semiconductor processing. With a minimal thickness of 100 nm and cross sections of up to 400 x 400 μm^2 the membranes offer extreme aspect ratios. Ion detection is demonstrated in MALDI-TOF analysis over a broad range from Insulin to BSA. The resulting data in detection shows much enhanced resolution as compared to existing detectors, which can offer better sensitivity and overall performance in resolving protein masses.

KEYWORDS

Nanomembranes, Protein detection, Mass spectrometry, Diamond ion detectors, Semiconductor

I. INTRODUCTION

The realization of nanomembranes with extreme lateral size generated a large demand in applications such as flexible displays, in medical diagnostics, and in chemical sensors [1,2]. Most of these applications focus on silicon, silicon-germanium, and III/V nanomembranes [3-6]. In early work we applied such silicon-based nanomembranes and realized their integration in MALDI-TOF MS units for protein detection in an extremely broad mass range with unprecedented resolution [4,7,9]. The principle of detection in this case is based on thermo-mechanics coupled with thermally driven field emission of electrons. The aim of this work is to employ CVD diamond as a detector material due to its ultimate mechanical and specific thermal properties. Here we make use of doped diamond, which by now is commercially available at high doping levels. In the following we demonstrate the fabrication and application of ultrathin freestanding diamond nanomembranes for the detection of large proteins.

The schematic configuration of our MALDI-TOF setup coupled with a diamond nanomembrane detector is illustrated in Fig. 1: the detector assembly is located at the exit of the time-of-flight line as in conventional MALDI-TOF systems. For the measurements

we used two MALDI-TOF units: a homemade system for calibration of the field emission properties and a commercial *Voyager-DE 530 STR* (*AB Sciex*). In operation the proteins are desorbed and ionized by a focused laser beam [10,11]. The ions are then accelerated to a final velocity depending on the mass m and charge state z by a large DC voltage (~ 25 kV). We note that all ions possess the same energy, since this is the quantity we are detecting. The differentiation according to the m/z ratio is obtained in the TOF-unit. Finally, the ions impact on the backside of the freestanding diamond namomembrane with a kinetic energy acquired in the initial acceleration stage [12]. The nanomembrane converts the kinetic energy into thermal energy and uses thermally driven field emission of electrons to detect the impact.

II. FABRICATION OF DIAMOND NANOMEMBRANES

The 100 nm thin freestanding diamond nanomembranes are fabricated from diamond-on-insulator (DOI) materials (*Advanced Diamond Technologies, Inc., Romeoville, IL, USA*) starting from optical lithography for defining the shape of the membranes. This step is followed by an etch step, which removes the support layers [8]. An optical micrograph of the 400×400 μm^2 freestanding, 100 nm thin boron doped (p-type) diamond nanomembrane used in this study is displayed in the inset of Fig. 1(b). The buckling pattern [13,14] in the

membrane is generated when the compressive residual stress is released [15,16] during etching out of the substrate layers within the defined square window [8].

III. ELECTRO-MECHANICAL CHARACTERIZATION OF NANOMEMBRANES

Before employing the nanomembrane for detection, we validated the applicability of the doped freestanding diamond nanomembranes as field emitters. We performed a set of measurements in vacuum using the experimental configuration shown in Fig. 2(a): the electric field is ramped between the diamond nanomembrane and the extraction gate by applying voltages to the membrane (V_{DM}) and the extraction gate (V_G). Increasing the electric field reduces the energy barrier for electrons inside the diamond membrane, making it easier for electrons to tunnel out [9,17,18]. The extraction grid funnels the electrons finally to the anode. In Fig. 2(b) the *IV*-characteristic of the 100 nm thin nanomembrane is given by red filled circles as a function of the voltage applied between the diamond membrane and extraction gate, V_{GM}.

In order to model the electron field emission analytically in this particular system, the mechanical and electrical behavior of the freestanding diamond nanomembrane need to be considered [4]. Effectively, the nanomembrane deforms due to the electromechanical

pressure exerted by applying V_{GM} [8]. Hence, the electric field strength between the membrane and the extraction gate is altered. The discrepancy in the intermediate voltage range can be explained with thermionic emission [19] and Schottky emission [17,20] as shown in the inset of Figure 2(b). The total emission consists of three distinct regions: the first one is at zero or at very small fields where thermionic emission acts over a barrier; the second one is the intermediate region of Schottky emission where the field is too low to cause Fowler-Nordheim (FN) tunneling [17,21-23] but it modifies the thermionic emission which works for fields up to around 10^7 V/m [17,20,24,25] (exactly the transition region in the curve); the final one is the region where FN tunneling takes over completely with fields above 10^7 V/m.

The Fowler-Nordheim (FN) equation [17] has been widely used to analyze field emission from diamond surfaces [41]. Chen *et al.* [24] developed a specific theoretical model for field emission from *p*-type diamond surfaces based on the theory of Stratton [42]. Following this model the total field emission current density from a freestanding boron-doped diamond nanomembrane can be modeled by [24, 25]

$$J = J_c + J_v = k_1 T^2 e^{-\frac{\theta}{kT}} e^{-k_2 \frac{\chi^{\frac{3}{2}}}{F}} + k_3 \frac{F^2}{\chi + E_g} e^{-k_2 \frac{(\chi + E_g)^{\frac{3}{2}}}{F}}, \quad (1)$$

where J_c and J_v are the emission current densities from the conduction band and the valence band, respectively, χ is the electron affinity, E_g is the energy gap, and θ is the energy difference between the surface conduction band minimum and the Fermi level,

$$k_1 = \frac{qmk^2}{2\pi^2 \mathrm{h}^3},\ k_2 = \frac{4\sqrt{2m}}{3q\mathrm{h}} v(y),\ k_3 = \frac{q^3}{16\pi^2 \mathrm{h}^2 t^2(y)},\ F = \beta \frac{V_{GM}}{s(V_{GM})}, \tag{2}$$

where $v(y)$ is a tabulated function involving an elliptic integral, $t(y)$ is another tabulated function closely related to $v(y)$ [43], and $s(V_{GM})$ is obtained from equation (S8).

Then, the total emission current from the freestanding diamond nanomembrane is proportional to the effective area of the surface and is given by $I = A_{eff} \times J$. The analytical plot of the total emission current from the 400×400 μm^2 freestanding 100 nm-thin diamond nanomembrane is depicted as a black line in Fig. 2(b).

Electron emission in the intermediate voltage range can be modeled as a combination of three emission mechanisms including thermionic emission, Schottky emission, and FN tunneling. Thermionic emission [19] is acting primarily in the range of very small electric fields and consists of electrons being thermally excited with sufficient energy to overcome the energy barrier at the surface and thus being emitted into vacuum. The thermionic

current is given by a well-known expression

$$J_{THc} = k_1 T^2 e^{\frac{-\theta}{k_B T}}, \tag{3}$$

where k_1 is the Richardson constant defined previously in Eq. (10).

Then, as the applied electric field increases, in the intermediate regime between thermionic emission and Fowler-Nordheim tunneling, a combination of the two effects occurs due to barrier lowering by the applied field. This intermediate region is where Schottky emission [20] plays a role for electron emission via modifying thermionic emission in the region where the electric field is not negligible, but it is not strong enough to cause FN tunneling:

$$J_{Sc} = k_1 T^2 e^{-\frac{\theta - \sqrt{\frac{Fe^3}{4\pi\varepsilon_0}}}{k_B T}}. \tag{4}$$

In this expression we can see how the applied electric field F, defined previously in (10), reduces the height of the barrier □ at the surface. Finally, FN tunneling [17] takes over completely and dominates electron emission at fields above 10^7 V/m, which, in our setup, occurs when the applied voltage exceeds 1500 V. FN tunneling is then modeled by the modified expression given previously in Eq. (1). A log-scale current fit taking into account the three components mentioned above is shown as a black-dashed line in the inset of Fig.

5(b). When combined together, the Eq. (1), Eq. (3), and Eq. (4) give a complete and accurate account of field emission from the nanomembrane. The resulting fit (a black dashed line in the inset of Fig. 2(b)) combining these three components matches the measurement data well. This exactly explains the mechanisms of field emission through the freestanding diamond membrane under applied electric fields.

IV. PROTEIN MEASUREMENTS WITH DIAMOND NANOMEMBRANES

In the next step we use the following proteins for testing the diamond nanomembrane as a detector for MALDI-TOF: Insulin with a mass of 5,735 Da, Cytochrome C at 12,365 Da, Apomyoglobin at 16,952 Da, Aldolase at 39,212 Da and finally Albumin (BSA) at 66,430 Da. As matrix solution we make use of standard sinapinic acid with a mass of 224 Da (*Sigma Aldrich, U.S.A.*) [8]. For the measurement, we set the accelerating voltage of the ion source to a standard of 25 kV and V_{GM}, the voltage difference between the diamond nanomembrane and the extraction gate to 2.3 kV. This value is based on the previously measured field emission characteristics, as shown in Fig. 2(b).

In order to demonstrate the performance of the diamond nanomembranes as mass spectrometers, we present the detection of Insulin and Cytochrome C with the datasets

shown in Fig. 2(c) and 2(d). The mass resolution obtained for Insulin and Cytochrome C is $m/\Delta m$ ~ 350 and ~ 438, respectively. The peak width Δm is defined by the standard full width at half maximum (FWHM) for a given mass (m). These resolutions are even better than those obtained from *(i)* Al/Si_3N_4/Al[4,7] where mass resolution for Insulin aprox. 100 m/dm and Cytochrome C aprox. 125 m/dm. Also, in *(ii)* Si-nanomembrane detector [9] where mass resolution for Insulin aprox. 50 m/dm and Cytochrome C aprox. 75 m/dm, and *(iii)* standard MCP detectors (as obtained in our MALDI-TOF unit for comparison) at a given mass range. This indicates the improved performance of diamond nanomembranes. The insets in (c) and (d) of Fig. 2 are the magnified views of the peak at the time-of-flight axis for Insulin and Cytochrome C, respectively. The peaks represent the sharp onset and the exponential decay as shown in a red-dashed line. The rise and decay time constant at the peak are 76.44 ns and 275.06 ns, respectively for Insulin. The peak for Cytochrome C shows 73.36 ns and 265.09 ns as the rise time and the decay time constant, respectively. The amplitudes of the peaks, rise times, and decay time constants in comparison are very similar for both proteins, since we have dialed in the same conditions such as concentration of proteins, initial accelerating high DC voltages, and the dimension of the nanomembrane. Specially, the mass resolution ($m/\Delta m$) increases rather than

decreases [26] for increased molecular masses owing to the time resolution being similar for all masses. The response time defined with the rise and decay time constants of the peak at time-of-flight axis results from thermal dissipation mechanisms within the membrane.

During the detection process, the nanomembrane is struck by the accelerated proteins from the MALDI-TOF unit, as depicted in Fig. 1: the proteins deposit their kinetic energy onto the membrane where this energy is absorbed (thermalized), causing a heating effect. The thermodynamics of the detection process control the observed field emission current of electrons, which is measured by the detector anode, after being accelerated by the extraction gate and amplified by the MCP. Inside the membrane, the thermal energy deposited on the backside by the proteins, is described as Q_{in} in Fig. 3(a), followed by a rapid transport of that thermal energy by lattice vibrations, or phonons, carrying the thermal energy across the membrane [9]. Since the phonon velocity in diamond is extremely high (~ 17,500 m/s) and the membrane thickness is smaller than the mean-free-path of phonons, the transit time of phonons across the 100 nm thick membrane is very short, on the order of 10 ps, and several orders of magnitude faster than either the duration of the impact of the protein cluster on the membrane or the response of the measured electron tunneling current observed in response to the MALDI-TOF measurement. Following the fast transit time of

quasi-ballistic phonons [27,28] across the membrane, the temperature at the opposite surface of the membrane rises due to the presence of additional heat-carrying phonons and causes an increase in the tunneling current of electrons due to the combined [19] thermally driven (thermionic) emission and gate-driven tunneling (field emission) effect, as shown by the peak in the field emission current density J in Fig. 3(a) and a corresponding peak in the membrane temperature T_{peak} in Fig 3(b).

The electron current is driven by both the elevated temperature caused by heating the membrane combined with the field emission produced by the applied external field. The combination of thermionic emission and field emission is given by Eq.(9), Eq.(12), and Eq.(13), where the presence of the $\sim T^2 e^{-\frac{\theta}{kT}}$ term implies a strong dependence of the electron current on temperature. The membrane is therefore a highly sensitive thermometer, producing a large tunneling current increase in response to the heating effect by the impacting proteins. As electrons leave the membrane via tunneling, they remove energy from the membrane, causing a cooling effect [29], which is captured as Q_{out} in Fig. 3(b). The total energy removed by the field emission process is $Q_{out}(T) = EJ(T,F)/e$, where e is the electron charge, E is the electron energy, and $J(T,F)$ is the temperature and field dependent total electron field emission current density, given by equations Eq.(9), Eq.(12),

and Eq.(13).

In addition to heat crossing the membrane laterally and being removed by electrons tunneling out of the membrane (Q_{out}), heat also diffuses laterally through the suspended membrane until it reaches the edges where the membrane is supported. We model the ballistic-diffusive transport of phonons in the nanomembrane by decomposing the problem into the normal (ballistic) and lateral (diffusive) direction, with the lateral heat diffusion being described by the heat equation with thermal conductivity calculated from the Boltzmann transport equation using full phonon dispersion and the phonon mean-free-path Λ. The details of our model are given in Supplemental information and are based on our previous work on silicon nanomembranes [9]. The resulting lateral thermal conductivity value is 12 W/(m*K) at room temperature, in agreement with experimental data on nanocrystalline diamond films [30]. The low value relative to single-crystalline diamond is caused by the reduction of the phonon mean-free-path due to scattering at the grain boundaries [31].

Results of the numerical simulation, in particular the electron current depicted in Fig. 3(a), match the shape, the rise time of ~75 ns, and the fall time of ~275 ns exhibited in the measured waveforms (shown in Fig. 2(c) and 2(d)), and show that the rise time is

determined mainly by the heating process of the impacting proteins. The deposited kinetic energy heats the nanomembrane until it reaches a point where electron field emission increases and begins to cool the membrane, as evidenced by the delay between Q_{in} and Q_{out} in Fig. 3(a) and 3(b). Consequently, the rise time of ~75 ns depends primarily on the duration of the impact of the proteins and not on the transit time of the phonons across the membrane. The decay time is limited by the slow lateral heat diffusion, as can be seen in the change of the peak temperature T_{peak} (see Figs. 3(b), 3(c) and 3(d)). The heat loss (cooling) Q_{out} via the thermionic emission of electrons is rapidly quenched due to its super-exponential dependence on temperature ($\sim T^2 e^{-\frac{\theta}{kT}}$), given by Eq. (9), (12), and (13). This strong temperature dependence of both J and Q_{out} explains the rapid initial drop in the electron tunneling current immediately following the impact of the proteins. What remains after J and Q_{out} (around ~1 μs in Fig. 3(a) and 3(b)) is slower process of heat diffusion in the lateral direction and the radiative heat loss to the environment.

V. DISCUSSION

Based on the simulations, we conclude that the combination of large aspect ratio, small grain structure [30,31] of the nanocrystalline diamond, and large phonon velocity combine to produce the rapid response by favoring the ballistic transport across the membrane and

limiting the heat loss in the lateral direction. The main advantage of the diamond nanomembrane as compared to silicon is their enhanced thermal conductivity. As we found in analyzing the DOI-material the diamond itself consists of nano-crystalline particles in a poly-crystalline matrix. These particles of about 50-nm diameter have a shape similar to rice grains and are aligned with their long axis perpendicular to the nanomembranes. Hence, heat transport in diamond nanomembranes is quite enhanced. However, the drawback is their mechanical fragility as compared to silicon and especially silicon-nitride membranes.

In summary we successfully demonstrated fabrication of ultra-thin CVD diamond nanomembranes with extremely large cross sections, followed by analysis of residual stress. We then investigated the field emission characteristics of doped freestanding diamond nanomembranes. The analytical description of field emission provides a detailed explanation of the dominating field emission mechanisms. We finally employed the nanomembranes in a commercial MALDI-TOF mass spectrometer detecting of various large proteins. The obtained data and theoretical analysis show a strongly improved sensitivity in terms of fast response time. This advanced response stems from the special thermo-mechanical characteristics of nanocrystalline CVD-grown diamond nanomembranes. This result offers the use of ultrathin-doped nanocrystalline diamond as an

outstanding material for protein detection at high mass.

Acknowledgements

We like to thank the Air Force Office of Scientific Research (AFOSR) for support through the MURI'08 (FA9550-08-1-0337). We also thank the Wisconsin Alumni Research Foundation (WARF) for support via an Accelerator Program grant and the Deutsche Forschungsgemeinschaft (DFG) for support via the Center for Ultrafast Imaging (CUI) under grant number EXC-1074 (B 1.3).

References

[1] K. Jenson, K. Kim, and A. Zettl, An atomic-resolution nanomechanical mass sensor, *Nat. Nanotechnol*. **3**, 533-537 (2008).

[2] M. S. Hanay, S. Kelber, A. K. Naik, D. Chi, S. Hentz, E. C. Bullard, E. Coline t, and L. Duraffourg, M. L. Roukes, Single-protein nanomechanical mass spectrometry in real time, *Nat. Nanotechnol*. **7**, 602-608 (2012).

[3] J. A. Rogers, M. G. Lagally, and R. G. Nuzzo, Synthesis, assembly and application of semiconductor nanomembranes, *Nature* **477**, 45-53 (2011).

[4] J. Park, H. Qin, M. Scalf, R. T. Hilger, M. S. Westphall, L. M. Smith, and R. H. Blick, A mechanical nanomembrane detector for time-of-flight mass spectrometry, *Nano Lett.* **11**, 3681-3684 (2011).

[5] S. Senapati, S. Basuray, Z. Slouka, L. J. Cheng, and H. C. Chang, A nanomembrane-based nucleic acid sensing platform for portable diagnostics, *Top. Curr. Chem*. **304**, 153-169 (2011).

[6] O. Ebil, A. S. Sharkawy, M. J. Zablocki, and D. W. Prather, Chemical and biological sensors based on nanomembrane technology, *Proc. SPIE* **7673**, 767308-1-767308-9 (2010).

[7] J. Park, H. Kim, and R. H. Blick, Quasi-dynamic mode of nanomembranes for time-of-flight mass spectrometry of proteins, *Nanoscale* **4**, 2543-2548 (2012).

[8] See Supplemental Material at [URL will be inserted by publisher] for theoretical aspects of nanomembranes fabrication and additional mass spectra.

[9] J. Park, Z. Aksamija, H. C. Shin, H. Kim, and R. H. Blick, Phonon-assisted field emission in silicon nanomembranes for time-of-flight mass spectrometry of proteins, *Nano Lett.* **13**, 2698-2703 (2013).

[10] W. C. Wiley, and I. H. McLaren, Time-of-flight mass spectrometer with improved resolution, *Rev. Sci. Instrum*. **26**, 1150-1157 (1955).

[11] K. Tanaka, H. Waki, Y. Ido, S. Akita, Y. Yoshida, and T. Yoshida, Protein and polymer analyses up to m/z 100,000 by laser ionization time-of-flight mass spectrometry, *Rapid Commun. Mass Spectrom*. **2**, 151-153 (1988).

[12] G. C. Hilton, Impact energy measurement in time-of-flight mass spectrometry with cryogenic microcalorimeters, *Nature* **391**, 672-675 (1998).

[13] T. Kramer, and O. Paul, Postbuckled micromachined square membranes under differential pressure, *J. Micromech. Microeng.* **12**, 475-478 (2002).

[14] A. Evans, M. Prestat, R. Tölke M. V. F. Schlupp, L. J. Gauckler, Y. Safa, T. Hocker, J. Courbat, D. Briand, N. F. De Rooij, and D. Courty, Residual stress and buckling patterns of free-standing Yttria-stabilized-zirconia membranes fabricated by pulse laser deposition, *Fuel Cells* **12**, 614-623 (2012).

[15] M. J. Madou, *Fundamentals of Microfabrication: The Science of Miniaturization*, (CRC Press, Boca Raton, 2002).

[16] J. A. Thornton, and D. Hoffman, Stress-related effects in thin films, *Thin Solid Films* **171**, 5-31 (1989).

[17] R. H. Fowler, and L Nordheim, Electron emission in intense electric fields, *Proc. R. Soc. London, Ser. A* **119**, 173-181 (1928).

[18] R. Stratton, Theory of field emission from semiconductors, *Phys. Rev.* **125**, 67-82 (1962).

[19] C. A. Mead. *J. Appl. Phys*, Operation of tunnel-emission devices, **32**, 646-652 (1961).

[20] F. Seitz, F. *Modern Theory of Solid* (McGraw-Hill Book Company, New York, 1940), Vol. 2, P. 161-168.

[21] T. Yamada, H. Yamaguchi, K. Okano, and A. Sawabe, Field emission properties of boron- and phosphorus-doped diamond, *New Diamond Front. Carbon Technol.* **15**, 337-347 (2005).

[22] P. T. Joseph, N. H. Tai, C. H. Chen, H. Niu, H. F. Cheng, and I. N. Lin, On the mechanism of enhancement on electron field emission properties for ultrananocrystalline diamond films due to ion implantation, *J. Phys. D: Appl. Phys.* **42**, 1-6 (2009).

[23] S. P. Bozeman, P. K. Baumann, V. L. Ward, M. J. Powers, J. J. Cuomo, R. J. Nemanich, and D. L. Dreifus, Electron emission measurements from CVD diamond surfaces, *Diamond Relat. Mater.* **5**, 802-806 (1996).

[24] C. L. Chen, C. S. Chen, and J. T. Lue, Field emission characteristic studies of chemical vapor deposited diamond films, *Solid State Electron.* **44**, 1733-1741 (2000).

[25] S. Y. Chen, and J. T. Lue, Temperature dependence of surface band bending and field emission for boron-doped diamond and diamond-like films, *New J. Phys.* **4**, 79.1-79.7 (2002).

[26] X. Chen, M. S. Westphall, and L. M. Smith, Mass spectrometric analysis of DNA mixtures: Instrumental effects responsible for decreased sensitivity with increasing mass, *Anal. Chem*. **75**, 5944-5952 (2003).

[27] M. E. Siemens, Q. Li, R. Yang, K. A. Nelson, E. H. Anderson, M. M. Murnane, and H. C. Kapteyn, Quasi-ballistic thermal transport from nanoscale interfaces observed using ultrafast coherent soft X-ray beams, *Nat. Mater*. **9**, 26-30 (2010).

[28] W. E. Bron, Y. B. Levinson, and J. M. O'Connor, Phonon propagation by quasidifussion, *Phys. Rev. Lett*. **49**, 209-211 (1982).

[29] M. S. Chung, S. C. Hong, A. Mayer, P. H. Cutler, B. L. Weiss, and N. M. Miskovsky, New analysis of electron energy exchange and cooling in semiconductors, *Appl. Phys. Lett*. **92**, 083505 (2008).

[30] H. Verhoeven, A. Floter, H. Reiss, R. Zachai, D. Wittorf, and W. Jager, Influence of the microstructure on the thermal properties of thin polycrystalline diamond films, *Appl. Phys. Lett*. **71**, 1329-1331 (1997).

[31] M. N. Touzelbaev, and K. E. Goodson, Application of micron-scale passive diamond layers for the integrated circuits and microelectromechanical systems industries, *Diamond Relat. Mater.* **7**, 1-14 (1998).

[32] K. Biswas, and K. S. Kal, Etch characteristics of KOH, TMAH and dual doped TMAH for bulk micromachining of silicon. *Microelectron. J.* **37**, 519-525 (2006).

[33] G. Yan, C. H. Chan Philip, I. M. Hsing, R. K. Sharma, J. K. O. Sin, and Y. Wang, An improved TMAH Si-etching solution without attacking exposed aluminum. *Sens. Actuators, A* **89**, 135-141 (2001).

[34] K. R. Williams, K. Gupta, and M. Wasilik, Etch rates for micromachining processing-Part II. *J. Microelectromech. Syst*. **12**, 761-778 (2003).

[35] A. Denisenko, A. Romanyuk, C., Pietzka, J. Scharpf, and E. Kohn, Surface damages in diamond by Ar/O_2 plasma and their effects on the electrical and electrochemical characteristics of boron-doped layers. *J. Appl. Phys*. **108**, 074901 (2010).

[36] W. K. Schomburg. *Introduction to Microsystem Design*, RWTH edn (Springer-Verlag, Berlin Heidelberg, 2011).

[37] D. Maier-Schneider, J. Maibach, and E. A. Obermeier, New analytical solution for the load-deflection of square membranes. *J. Microelectromech. Syst.* **4**, 238-241 (1995).

[38] C. Malhaire, A. Didiergeorges, M. Bouchardy, and D. Barbier, Mechanical characterization and reliability study of bistable SiO_2/Si membranes for microfluidic application. *Sens. Actuators A* **99**, 216-219 (2002).

[39] J. Park, H. Qin, M. Scalf, R. T. Hilger, M. S. Westphall, L. M. Smith, and R. H. Blick,

A mechanical nanomembrane detector for time-of-flight mass spectrometry. *Nano Lett.* **11**, 3681-3684 (2011).

[40] J. D. Jackson. *Classical Electrodynamics*, 2nd edn (John Wiley and Sons, New York, 1975).

[41] T. Yamada, H. Yamaguchi, K. Okano, and A. Sawabe, Field emission properties of boron- and phosphorus-doped diamond. *New Diamond Front. Carbon Technol.* **15**, 337-347 (2005).

[42] R. Stratton, Theory of field emission from semiconductors. *Phys. Rev.* **125**, 67-82 (1962)

[43] H. C. Miller, Values of Fowler-Nordheim field emission functions. *J. Franklin Inst*. **282**, 382-388 (1966).

[44] J. E. Graebner, M. E. Reiss, and L. Seibles, Phonon scattering in chemical-vapor-deposited diamond. *Phys. Rev. B* **50**, 3702-3713 (1994).

[45] Z. Aksamija, and I. Knezevic, Thermal conductivity of $Si_{1-x}Ge_x/Si_{1-y}Ge_y$ superlattices: Competition between interfacial and internal scattering. *Phys. Rev. B* **88**, 155318 (2013).

[46] L. Braginsky, N. Lukzen, V. Shklover, and H. Hofmann, High-temperature phonon thermal conductivity of nanostructures. *Phys. Rev. B* **66**, 134203 (2002).

[47] W. L. Liu, M. Shamsa, I. Calizo, and A. A. Balandin, Thermal conduction in nanocrystalline diamond films: Effects of the grain boundary scattering and nitrogen doping. *Appl. Phys. Lett*. **89**, 171915 (2006).

[48] C. Jeong, S. Datta, and M. Lundstrom, Thermal conductivity of bulk and thin-film silicon: A Landauer approach, *J. Appl. Phys*. **111**, 093708 (2012).

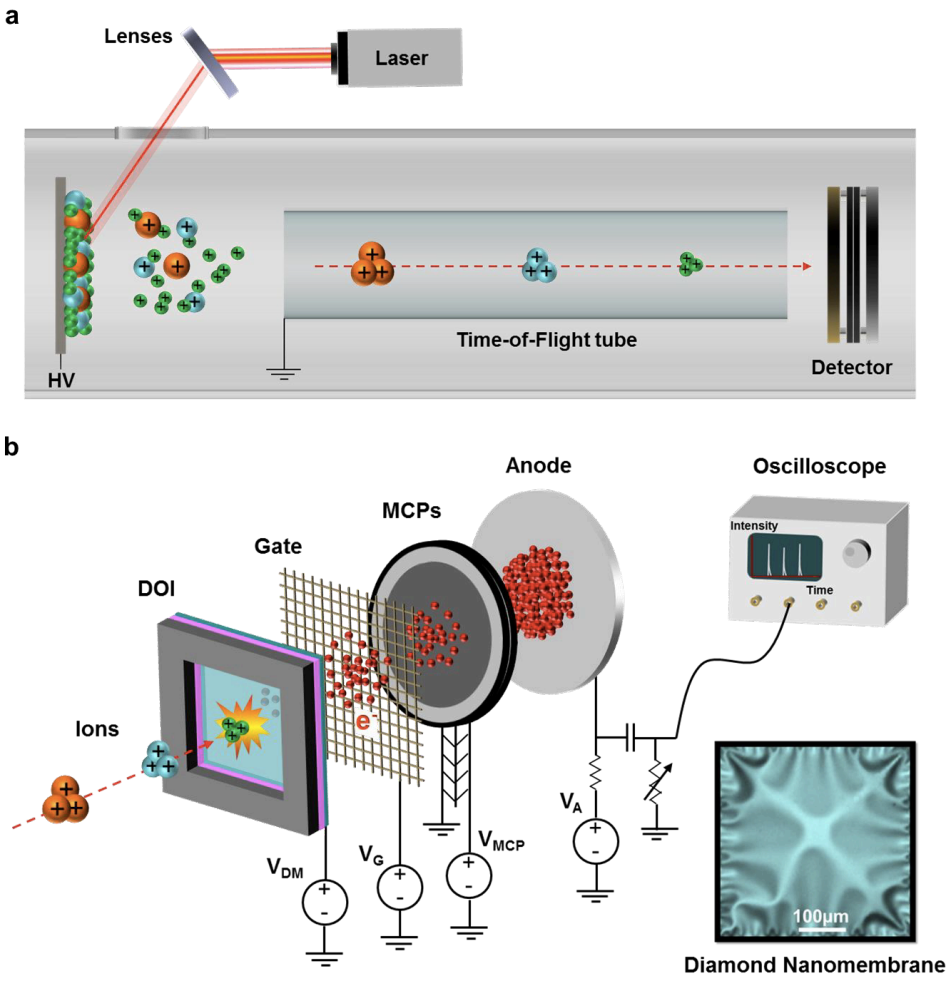

FIG. 1. The principle of operation of the diamond nanomembrane detector: (a**)** schematic of a MALDI-TOF mass spectrometer. Proteins are desorbed and ionized by MALDI, followed by a time-of-flight separation of proteins of different mass. (b**)** sketch of the detector configuration and operation principle. The detector consists of a freestanding diamond nanomembrane (receiving the kinetic energy of the impacting proteins), an extraction gate, MCP, and an anode. The electric field between the diamond nanomembrane and the extraction gate allows enhanced electron field emission by reducing the energy barrier, which electrons from inside the membrane have to overcome. The MCP amplifies the number of electrons, which pass through the extraction gate and arrive at the MCP. This flux of electrons is collected in the anode and the signal is traced on the oscilloscope in the time domain. The inset shows an optical microscope image of the 400×

400 μm^2 freestanding 100 nm-thick *p*-type diamond nanomembrane used for in this study. The buckling patterns in the membrane are generated when the compressive residual stress is released during processing.

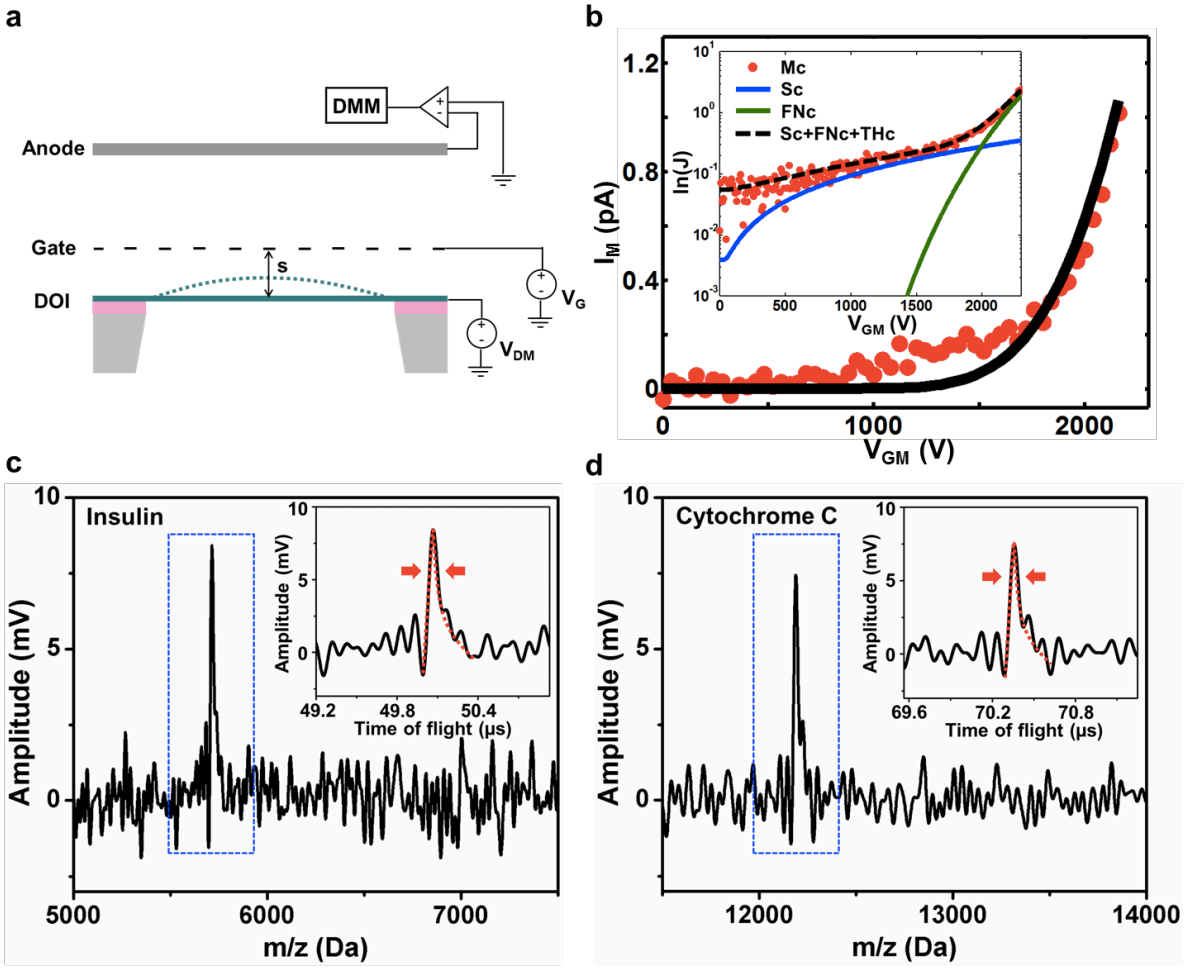

FIG. 2. Measurements with the diamond nanomembrane detector: (a) the schematic setup of the experimental configuration for field emission at room temperature. (b) Obtained data and analytical fits for field emission: the *IV*-curve of the measurement is given by the red filled circles, while the theoretical fit is shown as a black line. Inset: Log scale current analysis of the three distinct mechanisms of thermionic emission (THc), Schottky emission (Sc), and Fowler-Nordheim tunneling (FNc) and comparing this to the measurement (Mc)

in the intermediate voltage range. (c) and (d) show MALDI-TOF mass spectra of Insulin (5,735 Da) and Cytochrome C (12,365 Da), respectively. Insets in (c) and (d): the magnified view of the recorded peaks of Insulin and Cytochrome C, respectively. The shape of the peaks reveal a sharp onset due to quasi-diffusive transport of phonons in out-of-plane direction (normal to the surface of the membrane), and an exponential decay by the lateral heat diffusion along in-plane direction (across the membrane) as shown in a red-dashed line. The rise and decay time constants for Insulin are 76.44 ns and 275.06 ns, respectively. While the peak of Cytochrome C shows 73.36 ns and 265.09 ns. The peaks are very similar for both proteins since the protein concentrations, initial accelerating voltages, and of course the detecting nanomembranes are the same. The mass resolution ($m/\Delta m$) increases rather with increasing molecular mass. The mass resolution ($m/\Delta m$) obtained for Insulin and Cytochrome C is ~ 350 and ~ 480, respectively.

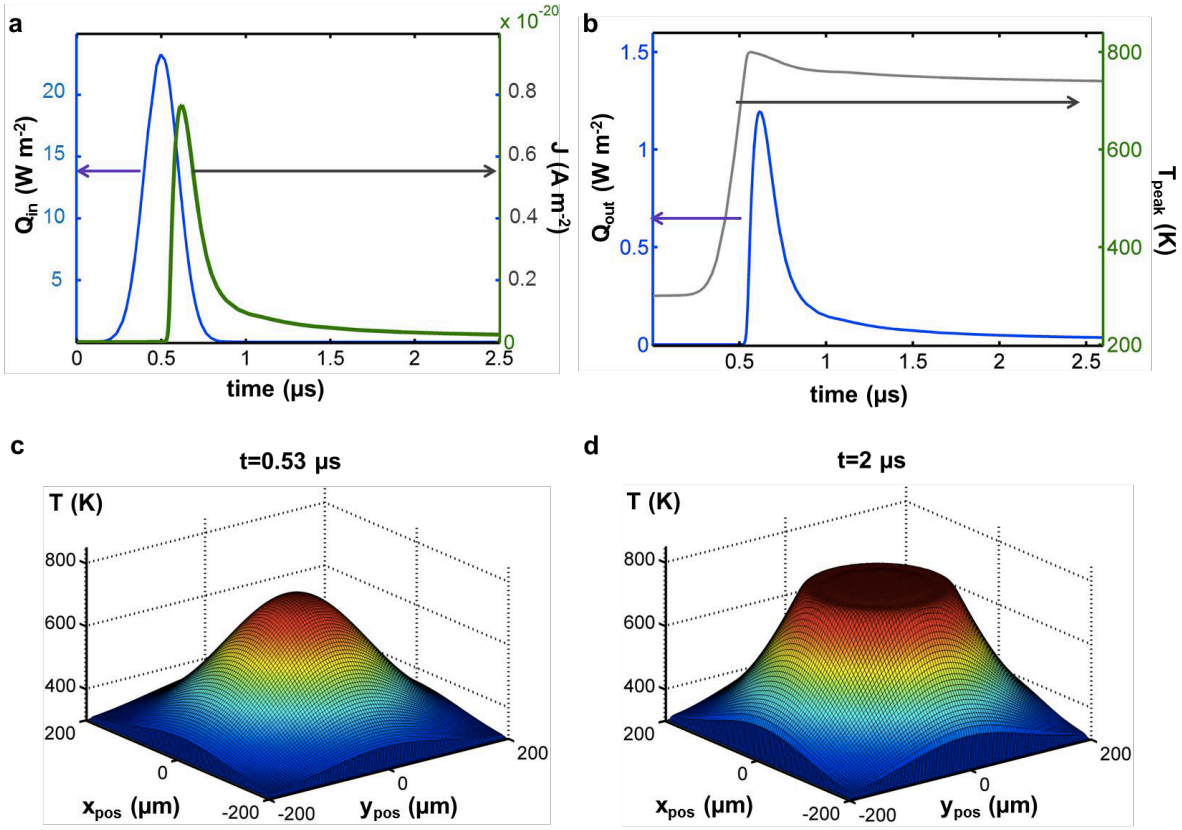

FIG. 3. Heat flux and temperature profile of the diamond nanomembrane, showing a plot of the heat input (Q_{in}) caused by the impact of the proteins and the resulting field emission

current J as a function of time (a). Field emission leads to an effective cooling, represented by the emitted heat (Q_{out}) in (b) which limits the peak temperature of the membrane to about 800 K. The heating is initially strongest in the center, as shown by the peak in (c) obtained at t = 0.53 μs which is the onset of the field emission current. After the field emission begins to cool the nanomembrane, the temperature profile flattens in the middle, as depicted in (d) at t = 2 μs, at the tail of the field emission peak, when the peak temperature has dropped below 800 K.